

A low-firing melilite ceramic $Ba_2CuGe_2O_7$ and compositional modulation on microwave dielectric properties through Mg substitution

Changzhi Yin

Guilin University of Technology

Zezong Yu

Nanchang University

Longlong Shu

Nanchang University

Laijun Liu

Guilin University of Technology

Yan Chen

Guilin University of Technology

Chunchun Li (✉ lichunchun2003@126.com)

Guilin University of Technology <https://orcid.org/0000-0002-3657-5856>

Research Article

Keywords: Ceramics, Dielectric properties, Melilite structure, Compositional modulation

Posted Date: July 2nd, 2020

DOI: <https://doi.org/10.21203/rs.3.rs-37521/v1>

License: © ⓘ This work is licensed under a Creative Commons Attribution 4.0 International License.

[Read Full License](#)

A low-firing melilite ceramic $\text{Ba}_2\text{CuGe}_2\text{O}_7$ and compositional modulation on microwave dielectric properties through Mg substitution

Changzhi Yin^{1,3#}, Zezong Yu^{2#}, Longlong Shu², Lijun Liu³, Yan Chen¹, Chunchun Li^{1,2,3*}

¹College of Information Science and Engineering, Guilin University of Technology, Guilin, 541004, China

²School of Materials Science and Engineering, Nanchang University, Nanchang 330031, People's Republic of China

³Guangxi universities key laboratory of non-ferrous metal oxide electronic functional materials and devices, College of Material Science and Engineering, Guilin University of Technology, Guilin, 541004, China

Abstract

A melilite $\text{Ba}_2\text{CuGe}_2\text{O}_7$ ceramic was characterized with low sintering temperature and moderate microwave dielectric properties. Sintered at 960 °C, the $\text{Ba}_2\text{CuGe}_2\text{O}_7$ ceramic had a high relative density 97%, a low relative permittivity 9.43, and a quality factor of 20,000 GHz. To get a deep understanding of the relationship between composition, structure, and dielectric performances, magnesium substitution for copper in $\text{Ba}_2\text{CuGe}_2\text{O}_7$ was conducted. Influences of magnesium doping on the sintering behavior, crystal structure, and microwave dielectric properties were studied. Mg doping in $\text{Ba}_2\text{CuGe}_2\text{O}_7$ caused negligible changes in the macroscopic crystal structure, grain morphology, and size distribution, while induced visible variation in the local structure as revealed by Raman analysis. Microwave dielectric properties exhibit a remarkable dependence on composition. On increasing the magnesium content, the dielectric constant (ϵ_r) featured a continuous decrease, while both the quality factor ($Q \times f$) and the temperature coefficient of resonance frequency (τ_f) increased monotonously. Such variations in dielectric performances were clarified in terms of the polarizability, packing fraction, and band valence theory.

Keywords: Ceramics; Dielectric properties; Melilite structure; Compositional modulation

these authors contribute equally as the first author

* Authors to whom correspondence should be addressed: lichunchun2003@126.com

1. Introduction

The development of wireless communication and broadband network technology has dramatically increased the demand for microwave dielectric materials, especially those being of small volume, low weight, high stability, and fast propagation speed. The primary performance parameters that should be concerned are: 1) suitable dielectric constants ϵ_r depending on specific application scenarios, 2) high quality factors $Q \times f$ (or low dielectric loss), and 3) low-temperature drift of the resonance frequency (τ_f) [1-3]. Particularly, the official commercialization of the fifth-generation (5G) networks is expanding the operational frequency to microwave and millimeter waves, and even terahertz bands [4, 5]. To realize rapid signal propagation under so high frequencies, low permittivity is a prerequisite given that the decay for electromagnetic signal transmission in dielectric carriers is in proportion to the relative permittivity [6].

Up to now, there have been many studies on the exploration of low- ϵ_r dielectric materials, most of which highlight silicates such as MgSiO_3 ($\epsilon_r = 6.7$), Zn_2SiO_4 ($\epsilon_r = 6.6$), and $\text{Ba}_2\text{ZnSi}_2\text{O}_7$ ($\epsilon_r = 8.09$) because of the low polarizability of silicon ($\sim 0.87 \text{ \AA}^3$) [7-9]. Among them, Si-based melilites with a chemical formula [$\text{A}_2\text{BSi}_2\text{O}_7$] have attracted intensive attention as microwave dielectric materials due to the ease with which the structures can accommodate different combinations of cations in the A and B sites [9-11]. The structure of $\text{A}_2\text{BSi}_2\text{O}_7$ melilite is represented as a two-dimensional framework of tetrahedral sheets of corner-sharing [SiO_4] and [BO_4] tetrahedra, in such a way that the [SiO_4] tetrahedra linked at one corner to form [Si_2O_7] dimers and the four remaining corners in the dimer are linked to the [BO_4] tetrahedra. Consequently, a set of distorted pentagonal rings is formed and the big A ions enter these sites, providing the connection between adjacent sheets [12, 13]. The compositional and structural flexibility of melilites provides wide space and potential for tunability in their physical properties. As regards, in our previous work, Ge substitution for Si was proposed to modify the sintering behavior and dielectric performance of $\text{A}_2\text{BSi}_2\text{O}_7$. Consequently, some Ge-based melilites $\text{A}_2\text{BGe}_2\text{O}_7$ (with A = Sr, Ba and B = Zn, Mg) have been reported to possess encouraging microwave dielectric properties with $\epsilon_r = 7.76\text{-}9.0$, $Q \times f = 13,950\text{-}35,700 \text{ GHz}$, and $\tau_f = -84.4 \sim -55 \text{ ppm/}^\circ\text{C}$ [14, 15].

Recent reports have featured that CuO, either as a low-melting-point (1086 °C) ingredient or as a sintering aid, usually facilitates sintering and updates dielectric behaviors [16, 17]. For example, adding appropriate amount of CuO in Mg₂SiO₄ stabilized the crystal structure and lowered the dielectric loss to some extent [18]. Wang et al. reported similar enhancement in sintering behavior and dielectric performances of Li₃Mg₂NbO₆ by CuO doping [19]. This inspires us to investigate whether Cu incorporation in the Ge-based melilites would further yield a reduction in sintering temperature and improvement in dielectric properties.

Herein, Ba₂CuGe₂O₇, a member of melilites, was studied on the dielectric properties at microwave frequencies with an attempt to explore novel materials as potential candidates for microwave communication. Besides, given the identical valence and effective ionic radius for Mg²⁺ and Cu²⁺ in a tetra-coordinated group, the substituted magnesium in Ba₂CuGe₂O₇ is expected to induce certain structural variation on either macroscopic or microscopic scale, which in turn engenders property evolutions. Doping effects on the sintering behavior, crystal structure, and microwave dielectric properties were studied.

2. Experimental

2.1 Materials synthesis

A simple solid-state route was employed to fabricate Ba₂Cu_{1-x}Mg_xGeO₇ ceramics ($x = 0, 0.2, 0.4, 0.6,$ and 0.8) using high-purity BaCO₃, CuO, GeO₂, and MgO (99.9%, Shanghai Aladdin, China) as raw materials, which were weighted according to the stoichiometry. Powder mixing via ball milling was conducted at a speed of 200 r/min for 4 h. After calcined at 900 °C for 4 h, the powders were secondly milled for particle uniformity, after which an appropriate amount of polyvinyl alcohol binder (5 wt.%) was added. Then green pellets were pressed into cylinders with a diameter of 12 mm and 6 mm of thickness under a uniaxial pressure of 100 MPa. Sintering behavior was performed in a temperature range from 900 °C to 1140 °C to achieve the best density, which was measured based on the Archimedes method.

2.2 Characterizations

The phase formation and purity were determined by X-ray diffraction using a Bruker Corporation

diffractometer (D8 ADVANCE03030502, Karlsruhe, Germany). The microstructures were performed on the polished and thermal etched surfaces of the $\text{Ba}_2\text{CuGe}_2\text{O}_7$ ceramics and measured by a scanning electron microscope (JSM-6701 F, Akishima City, Japan). Before SEM measurements, gold sputtering was done using a sputter coater (Ted Pella, America). Micro Raman Spectroscopy System (Witec, Ulm, Germany) is used for obtaining the Raman spectra with an argon ion laser ($\lambda = 514.5 \text{ nm}$) as the excitation light. Raman shifts were measured with a precision of $\approx 0.3 \text{ cm}^{-1}$. The spectral resolution is of the 1 cm^{-1} order and the range of it is $150\text{-}1200 \text{ cm}^{-1}$. Microwave dielectric properties were measured by a Vector Network Analyzer (Rohde & Schwarz, Munich, Germany). According to the Hakki-Coleman method, the dielectric constants (ϵ_r) and quality factor ($Q \times f$) were measured in the frequency range 10-16 GHz with a TE011 resonant mode. The temperature coefficient of resonance frequency (τ_f) was determined by recording the frequency drift over a temperature range from $25 \text{ }^\circ\text{C}$ to $85 \text{ }^\circ\text{C}$ in a temperature cavity.

3. Results and discussion

3.1 Crystal structure and dielectric properties of $\text{Ba}_2\text{CuGe}_2\text{O}_7$

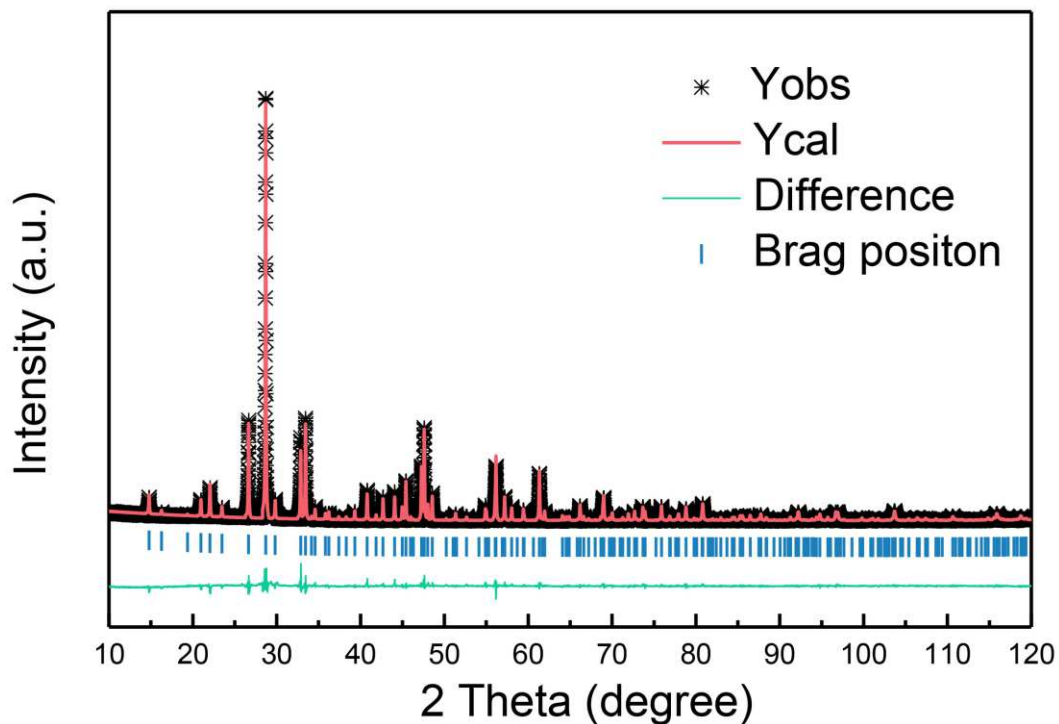


Figure 1 Room-temperature XRD pattern and Rietveld refinement plots for $\text{Ba}_2\text{CuGe}_2\text{O}_7$

Figure 1 shows the room-temperature XRD pattern and the calculated profile based on the Rietveld

refinement performed on the $\text{Ba}_2\text{CuGe}_2\text{O}_7$ ceramic sintered at 960 °C for 6 h. A tetragonal melilite structure model with space group $P-42_1m$ (113) was adopted for refinement. The calculated pattern fits well with the observed patterns, yielding low reliable factors with $R_p = 6.02\%$ and $R_{wp} = 7.73\%$. This result confirms the phase purity and the crystal structure of $\text{Ba}_2\text{CuGe}_2\text{O}_7$. The refined crystal parameters are $a = b = 8.5133 \text{ \AA}$, $c = 5.4495 \text{ \AA}$ and $V = 390.2468 \text{ \AA}^3$.

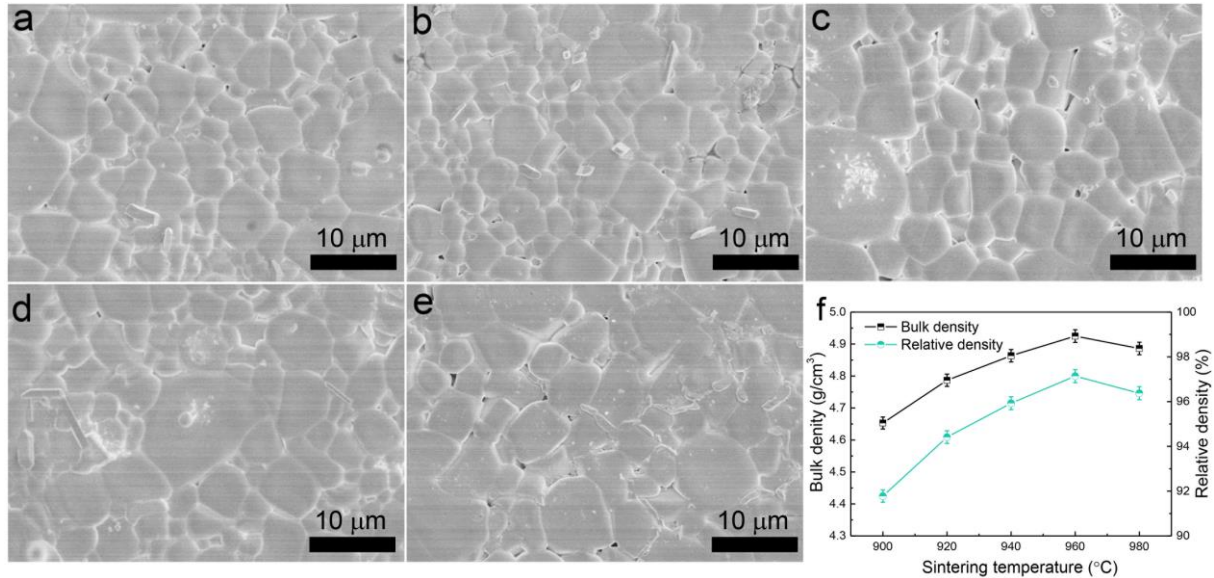


Figure 2 SEM micrographs of the polished and thermal etched surfaces of the $\text{Ba}_2\text{CuGe}_2\text{O}_7$ ceramics sintered at (a) 900 °C, (b) 920 °C, (c) 940 °C, (d) 960 °C, and (e) 980 °C; (f) the bulk density and relative density as a function of sintering temperature

To explore the sintering behavior of $\text{Ba}_2\text{CuGe}_2\text{O}_7$ ceramics, the microstructure evolution and density variation as a function of sintering temperature were recorded and shown in [Figure 2](#). Evident grain growth was detected accompanied by a decrease in porosity as the sintering temperature, both signature for densification. Consequently, a dense microstructure with grains about 5-7 μm was obtained after sintered at 960 °C ([Figure 2d](#)). Correspondingly, the density ([Figure 2f](#)) experienced an obvious increase from 4.65 g/cm^3 (~ 92% theoretical density) at 900 °C to 4.93 g/cm^3 (~ 97%) at 960 °C. The slight decrease in density (4.89 g/cm^3) when sintered at 980 °C might be related to the large grains that give rise to re-entrant pores, as shown in [Figure 2e](#).

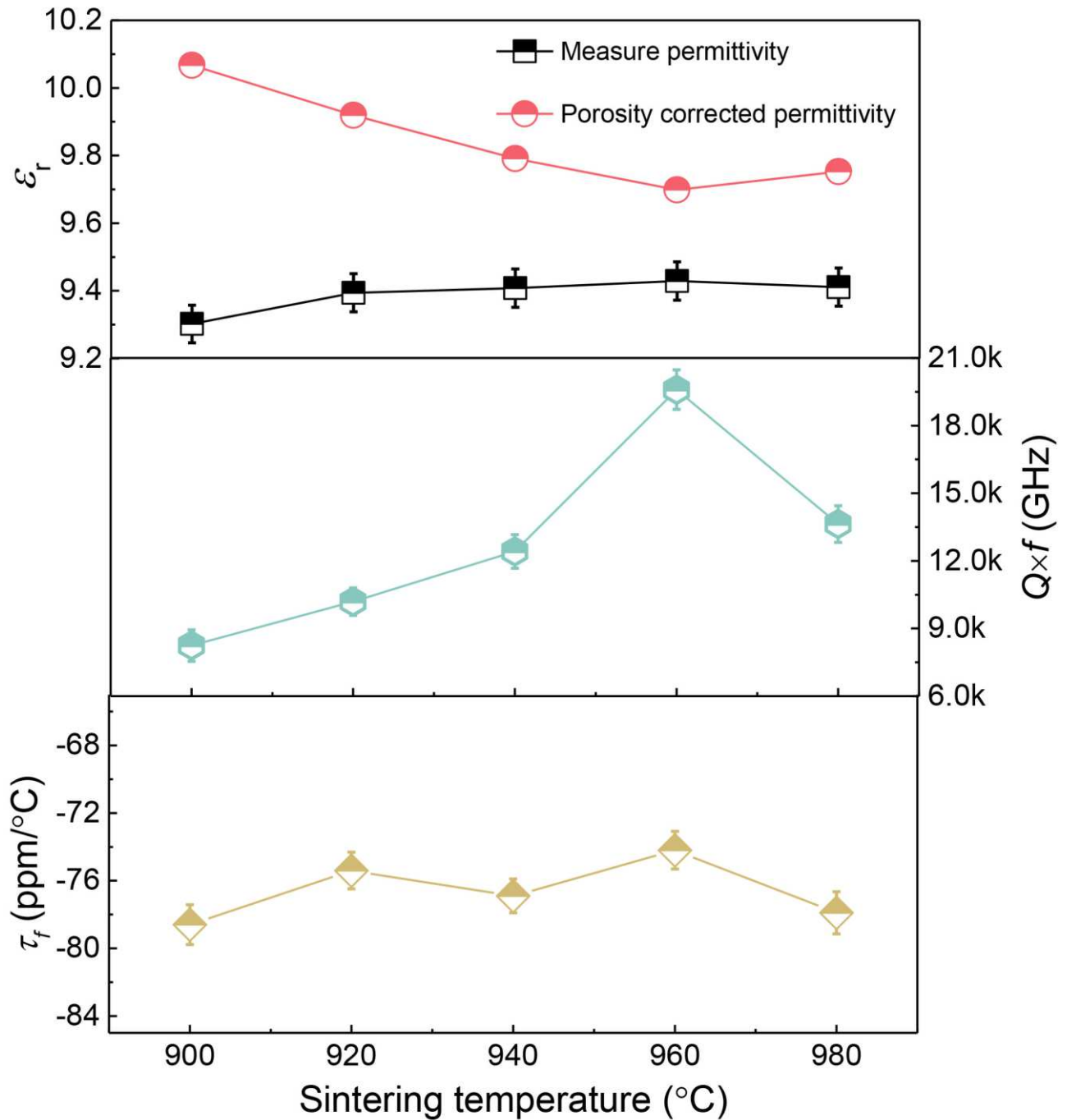


Figure 3 Microwave dielectric properties of $\text{Ba}_2\text{CuGe}_2\text{O}_7$ ceramics sintered at different temperatures (900- 980 °C)

Figure 3 shows the variations in the dielectric properties (ϵ_r , $Q \times f$, and τ_f) of the $\text{Ba}_2\text{CuGe}_2\text{O}_7$ ceramics sintered at a temperature range from 900 °C to 980 °C. As the sintering temperature increased both ϵ_r and $Q \times f$ revealed a similar change trend resembling the density (Figure 2f). A saturated value of $\epsilon_r \sim 9.43$ and $Q \times f \sim 20,000$ GHz was obtained in the sample sintered at 960 °C. It is well known that synergetic contributions from the extrinsic and intrinsic factors engender the overall variation in dielectric performances [20-22]. Herein, the strong correlation of the relative permittivity and quality factor on the density reveals a predominant role of density on the dielectric properties of $\text{Ba}_2\text{CuGe}_2\text{O}_7$. By contrast, the τ_f was weakly dependent on the sintering temperature, and fluctuated around -76 ppm/°C. In summary, a composition

sintered at 960 °C possessed the optimal microwave dielectric properties with $\epsilon_r = 9.43$, $Q \times f = 20,000$ GHz, and $\tau_f = -76$ ppm/°C. By comparison with $\text{Ba}_2\text{MgGe}_2\text{O}_7$ ($\epsilon_r = 7.76$, $Q \times f = 20,700$ GHz, and $\tau_f = -55$ ppm/°C), the present Cu-based compound has a higher permittivity, while its quality factor and the thermal stability of resonance frequency are inferior to those of $\text{Ba}_2\text{MgGe}_2\text{O}_7$. Thus, Mg substitution for Cu in $\text{Ba}_2\text{CuGe}_2\text{O}_7$ was conducted with an attempt to tune the dielectric performances of $\text{Ba}_2\text{CuGe}_2\text{O}_7$ and to correlate such dielectric evolutions to the composition and crystal structure.

3.2 Effects of magnesium substitution on crystal structure and microstructure

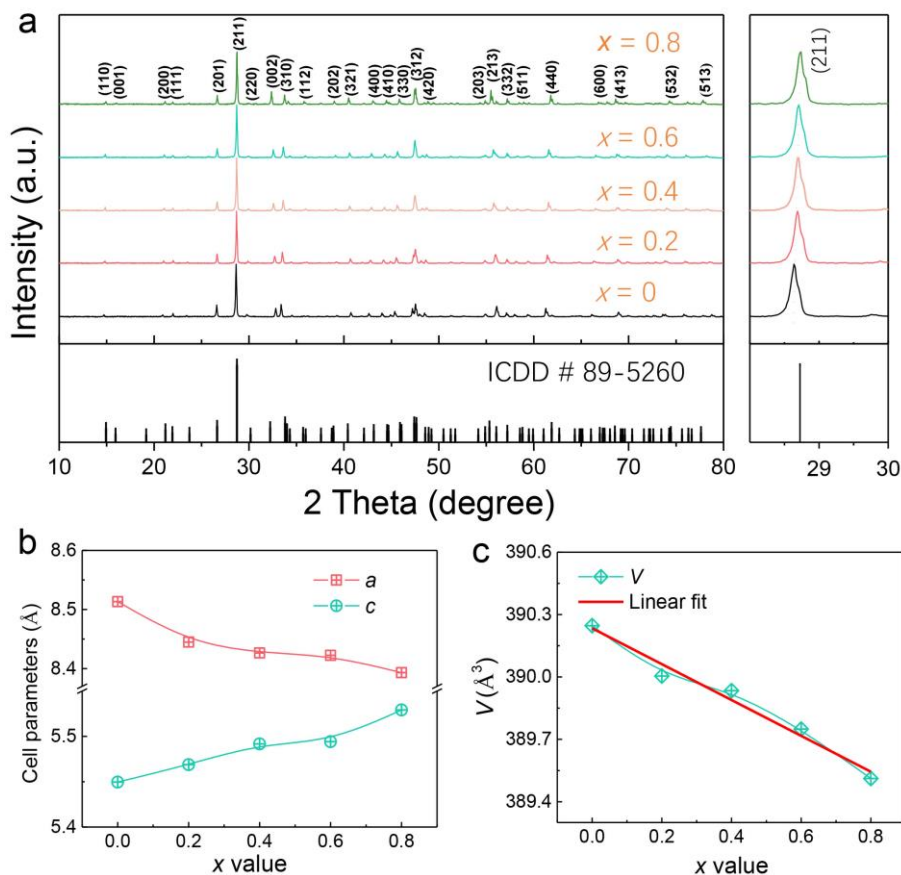


Figure 4 (a) Room-temperature XRD patterns for $\text{Ba}_2\text{Cu}_{1-x}\text{Mg}_x\text{Ge}_2\text{O}_7$ ($x = 0, 0.2, 0.4, 0.6$, and 0.8) powders calcined at 900 °C; (b, c) variations in the lattice parameters as a function of composition x .

The equivalent substitution of Mg for Cu caused no change in the macroscopic crystal structure of melilite $\text{Ba}_2\text{CuGe}_2\text{O}_7$ but indeed induced continuous variation in lattice parameters. Figure 4a shows XRD patterns recorded on the calcined $\text{Ba}_2\text{Cu}_{1-x}\text{Mg}_x\text{Ge}_2\text{O}_7$ ($x = 0, 0.2, 0.4, 0.6$, and 0.8) powders at 900 °C. A similar pattern is observed for all compositions and by indexing with ICDD # 89-5260 for $\text{Ba}_2\text{CuGe}_2\text{O}_7$, all peaks can be assigned and no additional peak is detected. The compositional-induced shift of (211) peak to the higher angle provides evidence of magnesium solution, despite the shift is not sizeable. The lattice parameters refined by

the least-square method are obtained from Rietveld refinements. As presented in [Figure 4b](#), an evident decrease in a is accompanied by a continuous increase in c , giving rise to a slight and monotonous decline in the unit cell by 0.18%. Otherwise, the linear variation in lattice parameters validates the Vegard's law for a solid solution. These results indicate the scheduled magnesium could completely dissolve into the lattice of melilite to form an infinite solid solution.

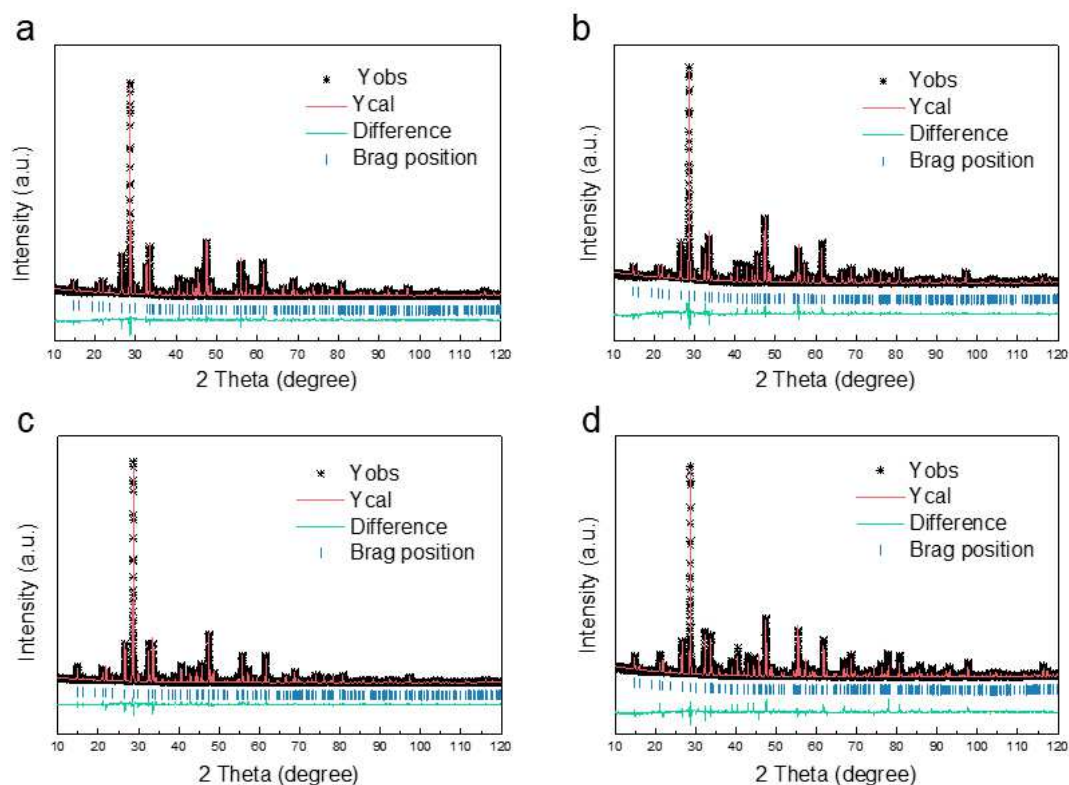


Figure 5 Rietveld refinement plots for $\text{Ba}_2\text{Cu}_{1-x}\text{Mg}_x\text{Ge}_2\text{O}_7$: (a) $x = 0.2$; (b) $x = 0.4$; (c) $x = 0.6$ and (d) $x = 0.8$.

Rietveld refinements, shown in [Figure 5](#), further verifying the phase purity and structural stability, are characterized by the good match between the calculated and experimental profiles and the reliable residual factors. It should be noted that the structural model was established based on the parent $\text{Ba}_2\text{CuGe}_2\text{O}_7$ and the sequences for refinements were set as scale factor, zero shift, background, lattice parameters, peak function parameters, and atomic positions, etc. Importantly, the atomic position for magnesium was fixed in the Cu positions and their distribution was set as random.

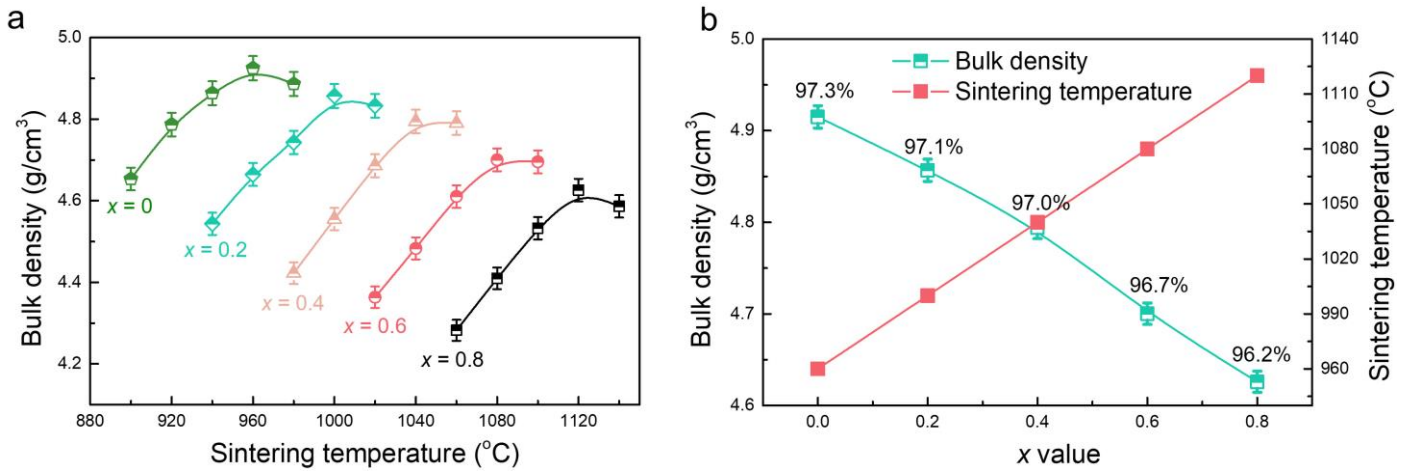


Figure 6 (a) Variations in bulk density as a function of sintering temperature for $\text{Ba}_2\text{Cu}_{1-x}\text{Mg}_x\text{Ge}_2\text{O}_7$; (b) the compositional dependence of bulk density and sintering temperature with the relative densities showing in the inset.

Figure 6 (a, b) illustrates the variation in bulk density as a function of sintering temperature and composition. All compositions exhibit an analogous dependence of the density on sintering temperature. An initial substantial increase in bulk density explains the crucial role of sintering temperature in promoting densification. A maximum bulk density (ρ_m) was achieved at a characteristic temperature (recognized as the optimized temperature, T_m) depending on composition. The compositional dependence of the ρ_m and T_m values is shown in Figure 6b, from which we can see that all compositions have a high relative density ($> 96\%$), suggesting they are applicable for subsequent dielectric characterizations. The much higher melting point of MgO (2852 °C) than that of CuO (1026 °C) accounts for the increase in sintering behavior.

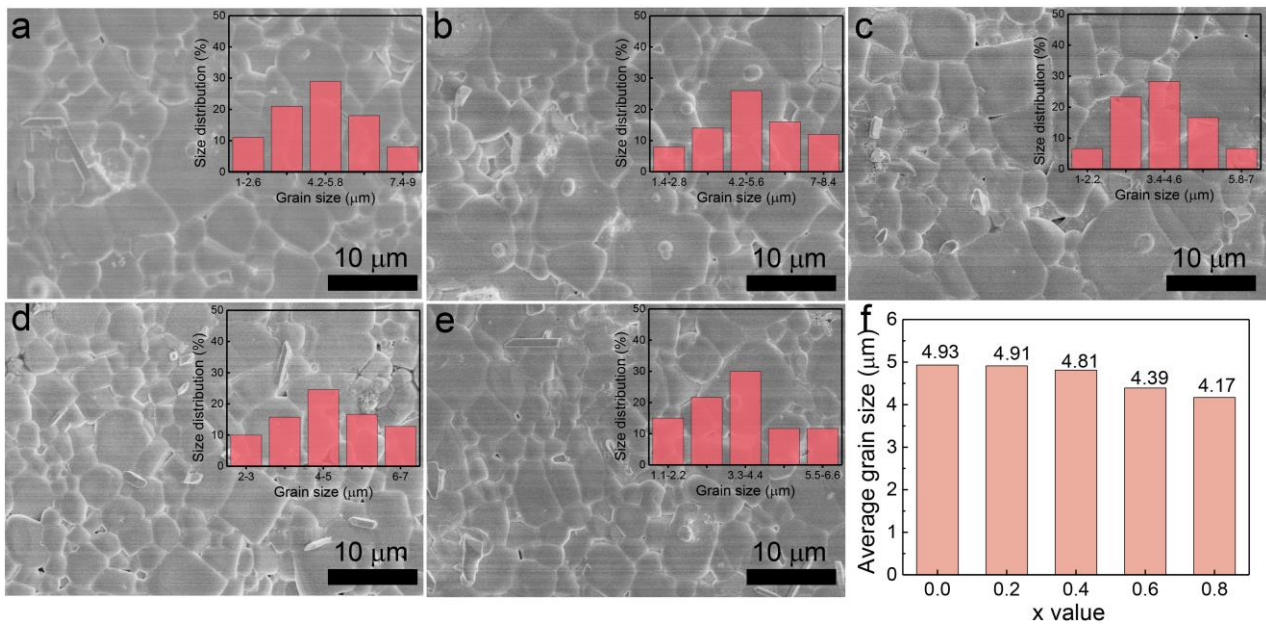


Figure 7 (a-e) SEM images and the grain size distributions for $\text{Ba}_2\text{Cu}_{1-x}\text{Mg}_x\text{Ge}_2\text{O}_7$ sintered at their optimum temperature; (f) the change of average grain size as a function of x value.

Figure 7 (a-e) shows SEM images of the polished and thermal etched surfaces of Mg-doped BCG along with their respective grain size distribution. Dense microstructures with few pores were developed for each compound, coincident with their high relative density. The similar grain morphology validated no structural transformation by Mg doping, which coincides with the XRD observation. Besides, the grain size distribution (in the inset of Figure 7) for all compounds is alike, giving rise to their close average grain size, as shown in Figure 7f.

Table 1 Wyckoff sites for atoms and the corresponding Raman active modes in $\text{Ba}_2\text{Cu}_{1-x}\text{Mg}_x\text{Ge}_2\text{O}_7$

Atom	Wyckoff site	Raman active modes
Ba	4e	$2A_1+B_1+2B_2+3E$
Cu (or Mg)	2a	B_1+B_2+2E
Ge	4e	$2A_1+B_1+2B_2+3E$
O	8f	$3A_1+3B_1+3B_2+6E$
2O	4e	$2A_1+B_1+2B_2+3E$
3O	2c	A_1+B_2+2E

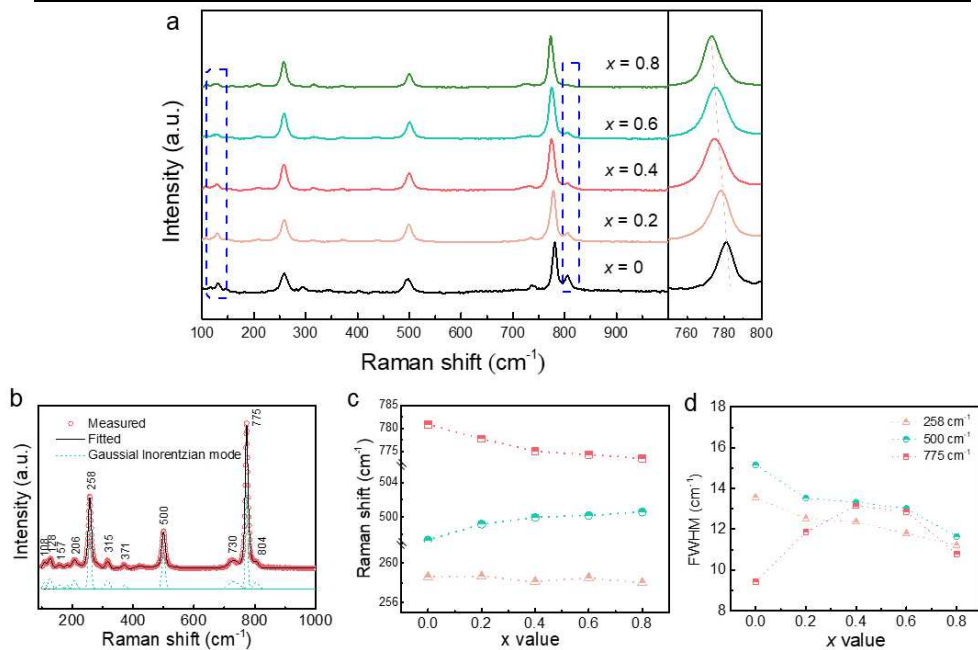


Figure 8 (a) Raman spectroscopies for $\text{Ba}_2\text{Cu}_{1-x}\text{Mg}_x\text{Ge}_2\text{O}_7$ along with an enlarged profile around 775 cm^{-1} ; (b) a representative deconvolution fitting for the $x = 0.8$ composition; (c, d) variations in the Raman shift and FWHM for the three strongest Raman modes at 775 cm^{-1} , 500 cm^{-1} , and 258 cm^{-1} .

Raman scattering is known to be highly sensitive to the local structure variations, especially those induced by composition [12, 23]. For a tetragonal $P-42_1m$ unit cell in $\text{Ba}_2\text{CuGe}_2\text{O}_7$, theoretically, the Raman active vibration modes are predicted based on the factor group theory and listed in Table 1 along with the Wyckoff sites. A total number of 45 ($\Gamma = 10A_1+7B_1+10B_2+18E$) Raman active modes are estimated. Figure 8a shows the room-temperature Raman spectra of the $\text{Ba}_2\text{Cu}_{1-x}\text{Mg}_x\text{Ge}_2\text{O}_7$ samples. Due to the low density and overlapping of some modes, only a limited number of Raman modes (11-16) are observed via the Gauss-Lorentzian deconvolution (Figure 8b), among which three strongest peaks appear around 775 cm^{-1} , 500 cm^{-1} , and 258 cm^{-1} , respectively. As well known, the Raman spectroscopy includes the internal vibrations of the framed polyhedron (either tetrahedron or octahedron for oxides) and the external ones from translational and librational moves [23]. Generally, the binding energy intra the polyhedral is larger than the intergroup or crystal energy, and thus the internal Raman modes usually appear at high-frequency bands. Thus, the strongest peak around 775 cm^{-1} is assigned as the symmetric stretching vibration of $[\text{GeO}_4]$, and the Raman mode around 500 cm^{-1} and 258 cm^{-1} corresponds to the asymmetric and symmetric bending of $[\text{GeO}_4]$, respectively. Nevertheless, the Raman modes related to the translation of $\text{Cu}^{2+} / \text{Mg}^{2+}$ locate around $200\text{-}225\text{ cm}^{-1}$ and $280\text{-}300\text{ cm}^{-1}$, as previously reported [12]. It should be noted that in the structure of melilite $\text{Ba}_2\text{CuGe}_2\text{O}_7$, the $[\text{CuO}_4]$ tetrahedra are corner-linked to the $[\text{Ge}_2\text{O}_7]$ dimers. Thus, the variation in the $[\text{CuO}_4]$ tetrahedra by Mg doping, either distortion/twisting or volume expansion/shrinkage would cause a corresponding change in the neighboring $[\text{GeO}_4]$ tetrahedra. Hence, by recording the alteration in the $[\text{GeO}_4]$ tetrahedra, the local structure evolution by Mg substitution can be manifested.

The change of Raman shift and the full width at half maximum (FWHM) of the strongest three modes are shown in Figure 8 (b, c). As shown, the 775 cm^{-1} mode is markedly red-shifted, while the 500 cm^{-1} and 258 cm^{-1} modes are quasi-invariant with increasing composition x . The red-shift in the 775 cm^{-1} mode indicates the decreased band energy of the $[\text{GeO}_4]$ tetrahedra. This can be explained by the increased bond length of Ge-O caused by the expansion in the $[\text{GeO}_4]$ because of the compress of the adjacent $[\text{Cu/MgO}_4]$ tetrahedra.

On the other hand, the width of the 500 cm^{-1} and 258 cm^{-1} modes monotonously decreased with increasing Mg content, while the 775 cm^{-1} mode was firstly broadened and then narrowed, resulting in the $x = 0.4$ composition featuring the highest FWHM. These results revealed that magnesium substitution induced local disorder, which becomes more distinct around $x = 0.4$.

More importantly, an extra mode in the parent $\text{Ba}_2\text{CuGe}_2\text{O}_7$ phase arises at 804 cm^{-1} and its intensity becomes weaker on the increasing magnesium content. This mode is assigned as the asymmetric stretching vibration of $[\text{GeO}_4]$. By comparing the Raman modes for $\text{Ba}_2\text{MgGe}_2\text{O}_7$ and $\text{Ba}_2\text{ZnGe}_2\text{O}_7$, a pretty evident difference lies in the absence or presence of this 804 cm^{-1} mode. In consideration of their same structure and atomic distribution, this distinction in Raman spectroscopy is believed to be related to the local structure distortion by Zn replacement for Mg. Similar phenomenon observed in this work validates the influences of magnesium substitution on the local structure.

In summary, magnesium substitution in $\text{Ba}_2\text{CuGe}_2\text{O}_7$ does not cause macroscopic phase transformation, or induce the second phase, or change the grain morphology and grain size distribution, but the evolutions in XRD peaks and Raman modes reveal that such doping indeed arouses local structural distortion, which could exert significant influences on dielectric properties.

3.3 Effects of magnesium substitution on dielectric properties

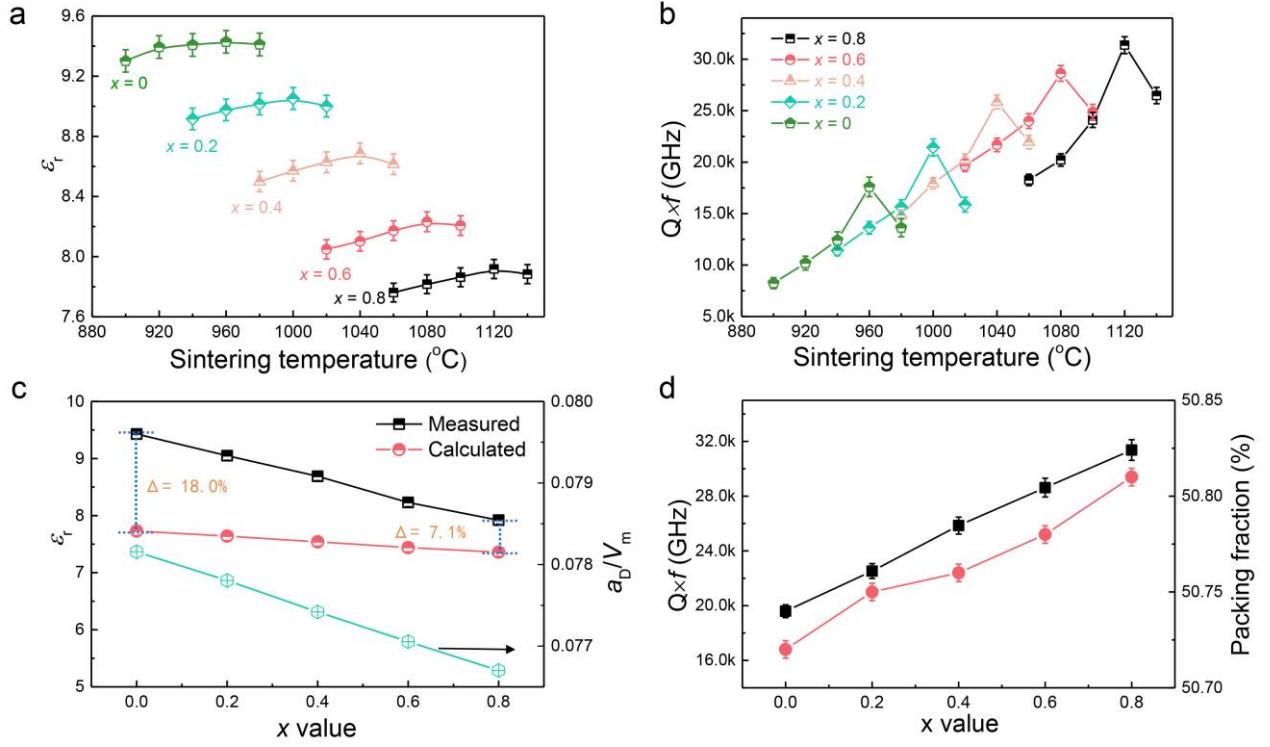


Figure 9 Variations in the relative permittivity (ϵ_r) and quality factor ($Q \times f$) of Ba₂Cu_{1-x}Mg_xGe₂O₇ (a, b) as a function of sintering temperature and (c, d) composition x value along with the change of the polarizability per unit volume (a_D^T/V_m) and packing fraction.

Figure 9 (a, b) represents the change of dielectric constants (ϵ_r) and quality factor ($Q \times f$) as a function of sintering temperatures. For each composition, both ϵ_r and $Q \times f$ value increased as the sintering temperature increased and then decreased slightly. Importantly, the variation tendency of ϵ_r and $Q \times f$ versus sintering temperature is similar to that of density, being an indicator for the crucial role of density on dielectric performances. Generally, the highest ϵ_r and $Q \times f$ values for each position are achieved in the densest sample. Figure 9 (c, d) summarizes the optimum ϵ_r and $Q \times f$ values for various compositions. Strong dependence on composition is visible for both quantities. Dielectric permittivity features a noticeable decrement with increasing Mg content from 9.05 at $x = 0$ to 7.92 at $x = 0.8$. Conversely, the quality factor exhibits a continuous rise from 20,000 GHz to 31,370 GHz as the amount of Mg increased from 0 to 0.8.

As well known, the dielectric permittivity and losses at microwave frequency bands not only depend on the intrinsic factors, but also the extrinsic ones from density (or pore), grain size, phase constitution, and phase transition, etc [20, 24-26]. Evidenced from the crystal structure and microstructure, magnesium substitution did not cause phase transformation, or induce the second phase, or change the grain morphology and grain

size distribution. Thus, effects from these extrinsic factors (density, grain size, phase transition, second phase) on the dielectric properties can be ruled out. Hence, it is rational to conclude that the compositional variation in dielectric permittivity and quality factor is mainly controlled by the intrinsic influences.

Theoretically, the dielectric permittivity is inherently affected by the molecular polarizability (α_D^T) and unit volume (V_m) based on the Clausius-Mossotti equation $\epsilon_r = (1 + 2b\alpha_D^T/V_m)/(1 - b\alpha_D^T/V_m)$ with $b = 4\pi/3$ as a constant, from which a direct correlation is accessible between ϵ_r and the polarizability per unit volume (α_D^T/V_m) [27]. The inset of Figure 9c shows the variation of α_D^T/V_m with composition, being characterized by a linear decrease. This result accounts for the underlying decrease of permittivity by magnesium substitution. Nevertheless, the calculated permittivities according to the Clausius-Mossotti equation are much smaller than the measured ones and the separation between them is about 7.1%-18.0%, decreasing with an increase of composition x , as shown in Figure 9c. Shannon ascribed such discrepancy as ionic or electronic conductivity, and/or structural distortion like rattling or compressed cations [27]. This large deviation, especially in $\text{Ba}_2\text{CuGe}_2\text{O}_7$, is an indicator of the local structural distortion and Mg doping released such distortion, which would inevitably influence the physical properties, e.g. dielectric properties.

Such local distortion on permittivity can be reflected by the bond characteristics estimated by the electronegativity difference (Δe). According to Pauling's rule [28], the electronegativity difference for $\text{Ba}_2\text{Cu}_{1-x}\text{Mg}_x\text{Ge}_2\text{O}_7$ is calculated as:

$$\Delta e = \frac{2\chi_{\text{Ba-O}} + (1-x)\chi_{\text{Cu-O}} + x\chi_{\text{Mg-O}} + 2\chi_{\text{Ge-O}}}{5} = \frac{9.5 + 0.59x}{5} \quad (1)$$

Evidently, the electronegativity difference increases linearly with increasing x value, and the Δe are calculated as 1.900, 1.924, 1.947, 1.971, and 1.994 for $x = 0$, $x = 0.2$, $x = 0.4$, $x = 0.6$, and $x = 0.8$, respectively. The smaller Δe than 2 indicates the covalent bond feature which becomes more prominent with Mg content. The enhanced covalent bond should in principle dilute the polarizability (or permittivity) because of the more rigid structure. However, an opposite variation trend in the relative permittivity validates the existence of some rattling or compressed cations rooting in the local distortion with an increase in Mg content.

The intrinsic influence on quality factor can be reflected by the packing fraction, as empirically summarized by Kim *et al.* [29, 30]. For a certain material system, the higher of the packing fraction, the smaller space for the thermal motion of cations or anions, thus leading to lower dielectric losses [31]. The packing fraction is defined as the total volume of packed ions over the volume of the unit cell and the calculated values are shown in Figure 9d. A consistent increase in packing fraction with the quality factor is seen because magnesium substitution in BCG heightened the packing fraction, leading to more close packing of ions, which in turn results in low dielectric losses. On the other hand, the release of local structural distortion with Mg doping partly accounts for the diminished dielectric loss.

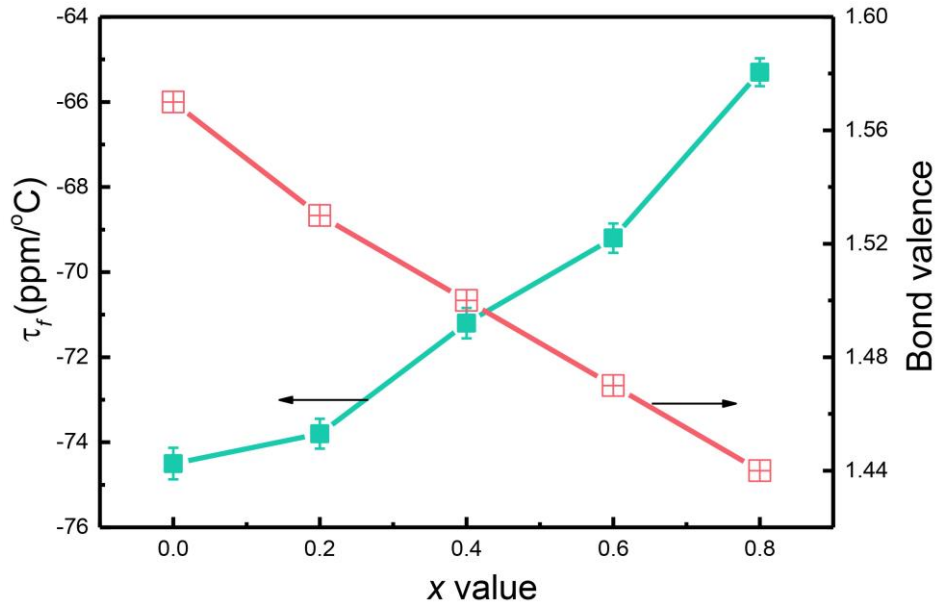


Figure 10 Variations in the temperature coefficient of resonance frequency (τ_f) and the bond valence of Mg/Cu-O.

A linear increase in the temperature coefficient of resonance frequency (τ_f) is illustrated in Figure 10 as the amount of Mg substitution increases from 0 to 0.8. It is well known that the τ_f value is correlated with the temperature coefficient of the relative permittivity (τ_ϵ) by the relation $\tau_f = -(\tau_\epsilon/2 + \alpha_L)$ (α_L represents the linear thermal expansion coefficient, which is usually a constant about 10 ppm/°C). Thereby, the composition dependence of τ_f can be analyzed by studying the respective variation in τ_ϵ value. Derived from the definition for τ_ϵ , Bosman and Havinga divided the formula as follows [32]:

$$\tau_\epsilon = \frac{1}{\epsilon} \left(\frac{\partial \epsilon}{\partial T} \right) = \frac{(\epsilon - 1)(\epsilon + 2)}{3\epsilon} (A + B + C)$$

$$\begin{aligned}
A &= \frac{1}{\alpha_m} \left(\frac{\partial \alpha_m}{\partial T} \right)_V \\
B &= \frac{1}{\alpha_m} \left(\frac{\partial \alpha_m}{\partial V} \right)_T \left(\frac{\partial V}{\partial T} \right)_P \\
C &= -\frac{1}{V} \left(\frac{\partial V}{\partial T} \right)_P
\end{aligned} \tag{2}$$

where ε and α_m represent the relative permittivity and polarizability, respectively. A is the direct dependence of the polarizability on temperature, being generally negative; B (generally positive) denotes the variation in polarizability concerning to the thermal change of volume, and C , in general negative, directly represents the volume change on temperature. The magnitude of the variables B and C are similar and in opposing signs. Hence, the relative magnitude between A and $(B+C)$ determines the signs and magnitude of τ_ε values. Particularly, both B and C terms involve in the volume variation, which would be reflected through the bond valence of ions. According to the previous reports on the calculation of bond valence [33-36], the Mg substitution effect on the bond valence of Cu-O in BCG is evaluated and shown in Figure 10. In contrast to the variation tendency in the τ_f value, a steady decrease occurs in the bond valence. The decreasing bond valence reveals the reduced structural distortion caused by magnesium doping. The thermal energy is preferential to recover the structural distortion, giving rise to a larger $(B+C)$ than A term, and thus a negative τ_f value. Therefore, the present rising τ_f value can be explained by the decrease in the structural distortion, as indicated by the decreased bond valence.

Table 2 The sintering temperature and microwave dielectric properties of some melilite structure ceramics

Ceramics	S.T. (°C)	Microwave properties		τ_f (ppm/°C)	Reference
		ε_r	$Q \times f$ (GHz)		
Ba ₂ ZnSi ₂ O ₇	1200	8.09	26,634	-51.46	[9]
BaCo ₂ Si ₂ O ₇	1060	9.26	31,135	-92.05	[10]
Ba ₂ MgGe ₂ O ₇	1280	7.76	20,700	-55	[14]

$\text{Ba}_2\text{ZnGe}_2\text{O}_7$	1180	9.0	13,950	-75	[14]
$\text{Sr}_2\text{MgGe}_2\text{O}_7$	1330	8.56	28,800	-70.5	[15]
$\text{Sr}_2\text{ZnGe}_2\text{O}_7$	1290	8.51	35700	-84.4	[15]
$\text{Sr}_2\text{CoSi}_2\text{O}_7$	1375	8.9	34000	-56.7	[37]
$\text{Sr}_2\text{MnSi}_2\text{O}_7$	1375	8.8	32000	-58.8	[37]
$\text{BaCu}_2\text{Si}_2\text{O}_7$	1025	8.29	46,085	-27.51	[38]
$\text{Ba}_2\text{CuGe}_2\text{O}_7$	960	9.43	20,000	-76	This work

Table 2 compares the sintering temperature and microwave dielectric properties of some melilite structured ceramics. As expected, either Si-based or Ge-based melilite compounds possess low permittivities ($\epsilon_r < 10$), moderate $Q \times f$ values, and negative τ_f values. Generally, Ba-containing compounds have relatively low sintering temperatures (~ 1200 °C), while those Sr-containing counterparts have higher sintering temperatures (> 1300 °C). What makes the present $\text{Ba}_2\text{CuGe}_2\text{O}_7$ unique is its lowest sintering temperature (960 °C) amongst the listed melilites, which makes it a potential candidate for LTCC technology when using Ag as the inner electrode [39-41].

4. Conclusions

In summary, we fabricated a series of magnesium substituted $\text{Ba}_2\text{CuGe}_2\text{O}_7$ ceramics and detailed the effects of magnesium on the sintering behavior, structure (both macroscopic and microscopic), and microwave dielectric properties. XRD and SEM results revealed that magnesium doping induced limited variations in the macroscopic structure and microstructure features. On the contrary, the densification temperature was remarkably raised from 960 °C to 1120 °C; meanwhile, Raman spectra provide an indicator of considerable change in the local structure, as characterized by the alteration in the Raman shift and width. Moreover, on increasing the magnesium content, the dielectric properties decreased from 9.43 to 7.92 which is attributed to the lower ionic polarizability of magnesium and the released local structural distortion, while the quality factor ($Q \times f$) increased from 19,560 to 31,370 GHz because of the increasing packing fraction. A monotonous

increase in τ_f was induced by magnesium substitution, which was explained by the decreased bond valence of Cu/Mg-O. This work provides a potential method to tune the thermal stability of $\text{Ba}_2\text{CuGeO}_7$ realized by increasing the bond strength through substituting larger cations, e.g. Ni^{2+} for Cu^{2+} or Si^{4+} for Ge^{4+} .

Acknowledgments

C.C. Li gratefully acknowledges the financial support from the Natural Science Foundation of Guangxi Zhuang Autonomous Region (No. 2018GXNSFAA281253) and high-level innovation team and outstanding scholar program of Guangxi institutes.

References

- [1] T. Sebastian, Dielectric materials for wireless communications. Elsevier Publishers, Oxford, U.K. 2008.
- [2] M.J. Wu, Y.C. Zhang, M.Q. Xiang, Synthesis, characterization and dielectric properties of a novel temperature stable $(1-x)\text{CoTiNb}_2\text{O}_8-x\text{ZnNb}_2\text{O}_6$ ceramic, *J. Adv. Ceram.* 8 (2019) 228-237.
- [3] C.C. Li, H.C. Xiang, M.Y. Xu, Y. Tang, L. Fang, Li_2AGeO_4 (A = Zn, Mg): Two novel low-permittivity microwave dielectric ceramics with olivine structure, *J. Eur. Ceram. Soc.* 38 (2018) 1524-1528.
- [4] Q.B. Lin, K.X. Song, B. Liu, H.B. Bafrooei, D. Zhou, W.T. Su, F. Shi, D.W. Wang, H.X. Lin, I.M. Reaney, Vibrational spectroscopy and microwave dielectric properties of $\text{AY}_2\text{Si}_3\text{O}_{10}$ (A = Sr, Ba) ceramics for 5G applications, *Ceram. Int.* 46 (2020) 1171-1177.
- [5] D. Zhou, L.X. Pang, D.W. Wang, C. Li, B.B. Jin, I.M. Reaney, High permittivity and low loss microwave dielectric suitable for 5G resonators and low temperature cofired ceramic architecture, *J. Mater. Chem.* 5 (2017) 10094-10098.
- [6] A. Ullah, H.X. Liu, H. Hao, J. Lqbal, Z.H. Yao, M.H. Cao, Influence of TiO_2 additive on sintering temperature and microwave dielectric properties of $\text{Mg}_{0.90}\text{Ni}_{0.1}\text{SiO}_3$ ceramics, *J. Eur. Ceram. Soc.* 37 (2017) 3045-3049.
- [7] M.E. Song, J.S. Kim, M.R. Joung, S. Nahm, Y.S. Kim, J.H. Paik, B.H. Choi, Synthesis and microwave dielectric properties of MgSiO_3 ceramics, *J. Am. Ceram. Soc.* 91 (2008) 2747-2750.
- [8] N.H. Nguyen, J.B. Lim, S. Nahm, J.H. Paik, J.H. Kim, Effect of Zn/Si ratio on the microstructural and microwave dielectric properties of Zn_2SiO_4 ceramics, *J. Am. Ceram. Soc.* 90 (2007) 3127-3130.
- [9] Z.Y. Zou, X.K. Lan, W.Z. Lu, G.F. Fan, X.H. Wang, X.C. Wang, P. Fu, W. Lei, Novel high curie temperature $\text{Ba}_2\text{ZnSi}_2\text{O}_7$ ferroelectrics with low-permittivity microwave dielectric properties, *Ceram. Int.* 42 (2016) 16387-16391.
- [10] X.Q. Song, W. Lei, M.Q. Xie, J. Li, X.C. Wang, W.Z. Lu, Sintering behaviour, lattice energy and microwave dielectric properties of melilite-type $\text{BaCo}_2\text{Si}_2\text{O}_7$ ceramics, *Mater. Res. Express* 6 (2020) 126322.
- [11] Z.Y. Zou, Z.H. Chen, X.K. Lan, W.Z. Lu, B. Ullah, X.H. Wang, W. Lei, Weak ferroelectricity and low-permittivity microwave dielectric properties of $\text{Ba}_2\text{Zn}_{(1+x)}\text{Si}_2\text{O}_{(7+x)}$ ceramics, *J. Eur. Ceram. Soc.* 37 (2017) 3065-3071.
- [12] J. Hanuza, M. Maćzka, M. Ptak, J. Lorenc, K. Hermanowicz, P. Becker, L. Bohatý, A. Kaminskii, Polarized IR and Raman spectra, temperature dependence of phonons and lattice dynamic calculations for $\text{M}'_2\text{M}''\text{Ge}_2\text{O}_7$ pyrogermanates ($\text{M}' = \text{Sr, Ba}$; $\text{M}'' = \text{Mg, Zn}$), *J. Raman Spectrosc.* 42 (2011) 782-789.
- [13] A. Sazonov, V. Hutanu, M. Meven, G. Roth, R. Georgii, T. Masuda, B. Náfrádi, Crystal Structure of magnetoelectric $\text{Ba}_2\text{MnGe}_2\text{O}_7$ at room and low temperatures by neutron diffraction, *Inorg. Chem.* 57 (2018) 5089.
- [14] C.C. Li, C.Z. Yin, J.Q. Chen, H.C. Xiang, Y. Tang, L. Fang, Crystal structure and dielectric properties of germanate melilites $\text{Ba}_2\text{MGe}_2\text{O}_7$ (M = Mg and Zn) with low permittivity, *J. Eur. Ceram. Soc.* 38 (2018) 5246-5251.
- [15] C.Z. Yin, Y. Tang, J.Q. Chen, F.H. Li, Y.J. Huang, C.C. Li, X.R. Xing, L. Fang, Two low-permittivity melilite ceramics in the SrO-MO-GeO_2 (M = Mg, Zn) system and their temperature stability through compositional modifications, *J. Eur. Ceram. Soc.* 40 (2020) 1186-1190.
- [16] Y.M. Lai, H. Su, G. Wang, X.L. Tang, X.F. Liang, X. Huang, Y.X. Li, H.W. Zhang, C. Ye, X.R. Wang, Improved microwave dielectric properties of $\text{CaMgSi}_2\text{O}_6$ ceramics through CuO doping, *J. Alloys Compd.* 772 (2019) 40-48.
- [17] L.X. Pang, D. Zhou, Microwave dielectric properties of low-firing Li_2MO_3 (M = Ti, Zr, Sn) ceramics with B_2O_3 -CuO addition, *J. Am. Ceram. Soc.* 93 (2010) 3614-3617.
- [18] Y.M. Lai, X.L. Tang, X. Huang, H.W. Zhang, X.F. Liang, J. Li, H. Su, Phase composition, crystal structure and microwave dielectric properties of $\text{Mg}_{2-x}\text{Cu}_x\text{SiO}_4$ ceramics, *J. Eur. Ceram. Soc.* 38 (2018) 1508-1516.
- [19] G. Wang, D.N. Zhang, F. Xu, X. Huang, Y. Yang, G.W. Gan, Y.M. Lai, Y.H. Rao, C. Liu, J. Li, L.C. Jin, H.W. Zhang, Correlation between crystal structure and modified microwave dielectric characteristics of Cu^{2+} substituted $\text{Li}_3\text{Mg}_2\text{NbO}_6$ ceramics, *Ceram. Int.* 45 (2019) 10170-10175.
- [20] E.S. Kim, N.S. Chun, K.H. Yoon, Dielectric properties of $[\text{Ca}_{1-x}(\text{Li}_{1/2}\text{Nd}_{1/2})_x]_{1-y}\text{Zn}_y\text{TiO}_3$ ceramics at microwave frequencies, *Mater. Sci. Eng. B* 99 (2003) 93-97.
- [21] C.Z. Yin, H.C. Xiang, C.C. Li, H. Porwal, L. Fang, Low-temperature sintering and thermal stability of Li_2GeO_3 -based microwave dielectric ceramics with low permittivity, *J. Am. Ceram. Soc.* 101 (2018) 4608-4614.

- [22] W.S. Kim, E.S. Kim, K.H. Yoon, Effects of Sm^{3+} substitution on dielectric properties of $\text{Ca}_{1-x}\text{Sm}_{2x/3}\text{TiO}_3$ ceramics at microwave frequencies, *J. Am. Ceram. Soc.* 82 (1999) 2111-2115.
- [23] F. Shi, H.L. Dong, Vibrational modes and structural characteristics of $(\text{Ba}_{(0.3)}\text{Sr}_{(0.7)})[(\text{Zn}_x\text{Mg}_{(1-x)})(1/3)\text{Nb}_{(2/3)}]\text{O}_3$ solid solutions, *Dalton Trans.* 40 (2011) 11591-11598.
- [24] A. Manan, Z. Ullah, A.S. Ahmad, A. Ullah, D.F. Khan, A. Hussain, M.U. Khan, Phase microstructure evaluation and microwave dielectric properties of $(1-x)\text{Mg}_{0.95}\text{Ni}_{0.05}\text{Ti}_{0.98}\text{Zr}_{0.02}\text{O}_{3-x}\text{Ca}_{0.6}\text{La}_{0.8/3}\text{TiO}_3$ ceramics, *J. Adv. Ceram.* 7 (2018) 72-78.
- [25] X.Q. Song, W.Z. Lu, X.C. Wang, X.H. Wang, G.F. Fan, R. Muhammad, W. Lei, Sintering behaviour and microwave dielectric properties of $\text{BaAl}_{2-2x}(\text{ZnSi})_x\text{Si}_2\text{O}_8$ ceramics, *J. Eur. Ceram. Soc.* 38 (2018) 1529-1534.
- [26] H.L. Pan, L. Cheng, H.T. Wu, Relationships between crystal structure and microwave dielectric properties of $\text{Li}_2(\text{Mg}_{1-x}\text{Co}_x)_3\text{TiO}_6$ ($0 \leq x \leq 0.4$) ceramics, *Ceram. Int.* 43 (2017) 15018-15026.
- [27] R.D. Shannon, Dielectric polarizabilities of ions in oxides and fluorides, *J. Appl. Phys.* 73 (1993) 348-366.
- [28] A.L. Allred, Electronegativity values from thermochemical data, *J. Inorg. Nucl. Chem.* 17 (1961) 215-221.
- [29] E.S. Kim, B.S. Chun, R. Freer, R.J. Cernik, Effects of packing fraction and bond valence on microwave dielectric properties of $\text{A}^{2+}\text{B}^{6+}\text{O}_4$ (A^{2+} : Ca, Pb, Ba; B^{6+} : Mo, W) ceramics, *J. Eur. Ceram. Soc.* 30 (2010) 1731-1736.
- [30] Q.W. Liao, L.X. Li, E. Xiang, D. Xiang, New low-loss microwave dielectric material $\text{ZnTiNb}_2\text{O}_8$, *J. Am. Ceram. Soc.* 94 (2011) 3237-3240.
- [31] M. Xiao, Q.Q. Guo, Z.Q. Zhou, P. Zhang, Study of the microwave dielectric properties of $(\text{La}_{1-x}\text{Sm}_x)\text{NbO}_4$ ($x = 0-0.10$) ceramics via bond valence and packing fraction, *J. Am. Ceram. Soc.* 100 (2017) 3952-3960.
- [32] H.L. Pan, L. Cheng, H.T. Wu, Relationships between crystal structure and microwave dielectric properties of $\text{Li}_2(\text{Mg}_{1-x}\text{Co}_x)_3\text{TiO}_6$ ($0 \leq x \leq 0.4$) ceramics, *Ceram. Int.* 43 (2017) 15018-15026.
- [33] H.S. Park, K.H. Yoon, E.S. Kim, Relationship between the bond valence and the temperature coefficient of the resonant frequency in the complex perovskite $(\text{Pb}_{1-x}\text{Ca}_x)[\text{Fe}_{0.5}(\text{Nb}_{1-y}\text{Ta}_y)_{0.5}]\text{O}_3$, *J. Am. Ceram. Soc.* 84 (2010) 99-103.
- [34] N.E. Brese, M. O'keeffe, Bond-valence parameters for solids, *International Union of Crystallography* 47 (1991) 192-197.
- [35] I.D. Brown, D. Altermatt, Bond-valence parameters obtained from a systematic analysis of the Inorganic Crystal Structure Database, *Acta Crystallogr., Sect. B* 41 (1985) 244-247.
- [36] E.S. Kim, S.H. Kim, Effects of structural characteristics on microwave dielectric properties of $(1-x)\text{CaWO}_{4-x}\text{LaNbO}_4$ ceramics, *J. Electroceram.* 17 (2006) 471-477.
- [37] T. Joseph, M.T. Sebastian, Microwave dielectric properties of $(\text{Sr}_{1-x}\text{A}_x)_2(\text{Zn}_{1-x}\text{B}_x)\text{Si}_2\text{O}_7$ ceramics ($\text{A} = \text{Ca}, \text{Ba}$ and $\text{B} = \text{Co}, \text{Mg}, \text{Mn}, \text{Ni}$), *J. Am. Ceram. Soc.* 93 (2010) 147-154.
- [38] X.Q. Song, Z.Y. Zou, W.Z. Lu, T. Chen, S.W. Ta, Z.X. Fu, W. Lei, Crystal structure, lattice energy and microwave dielectric properties of melilite-type $\text{Ba}_{1-x}\text{Sr}_x\text{Cu}_2\text{Si}_2\text{O}_7$ solid solutions, *J. Alloys Compd.* 835 (2020) 155340.
- [39] H.I. Hsiang, C.C. Chen, S.Y. Yang, Microwave dielectric properties of $\text{Ca}_{0.7}\text{Nd}_{0.2}\text{TiO}_3$ ceramic-filled $\text{CaO-B}_2\text{O}_3\text{-SiO}_2$ glass for LTCC applications, *J. Adv. Ceram.* 8 (2019) 345-351.
- [40] J. Zhou, Towards rational design of low-temperature co-fired ceramic (LTCC) materials, *J. Adv. Ceram.* 1 (2012) 89-99.

Figures

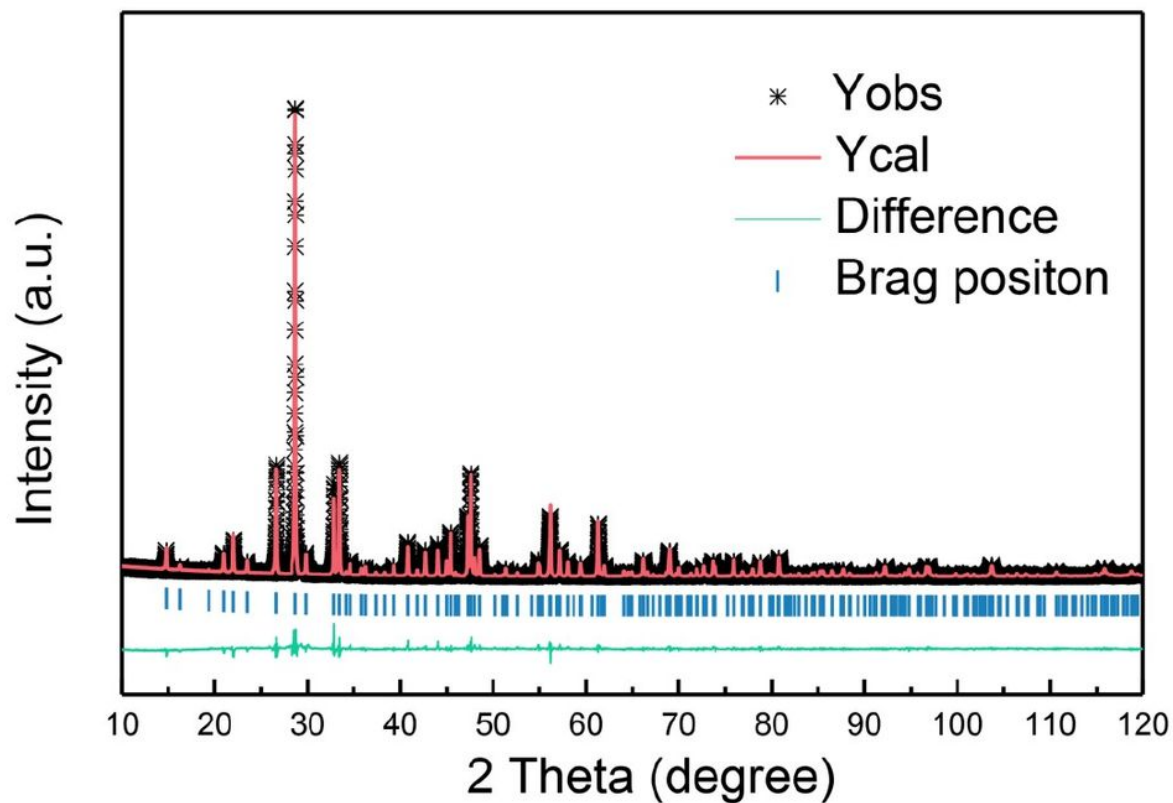


Figure 1

Room-temperature XRD pattern and Rietveld refinement plots for Ba₂CuGe₂O₇

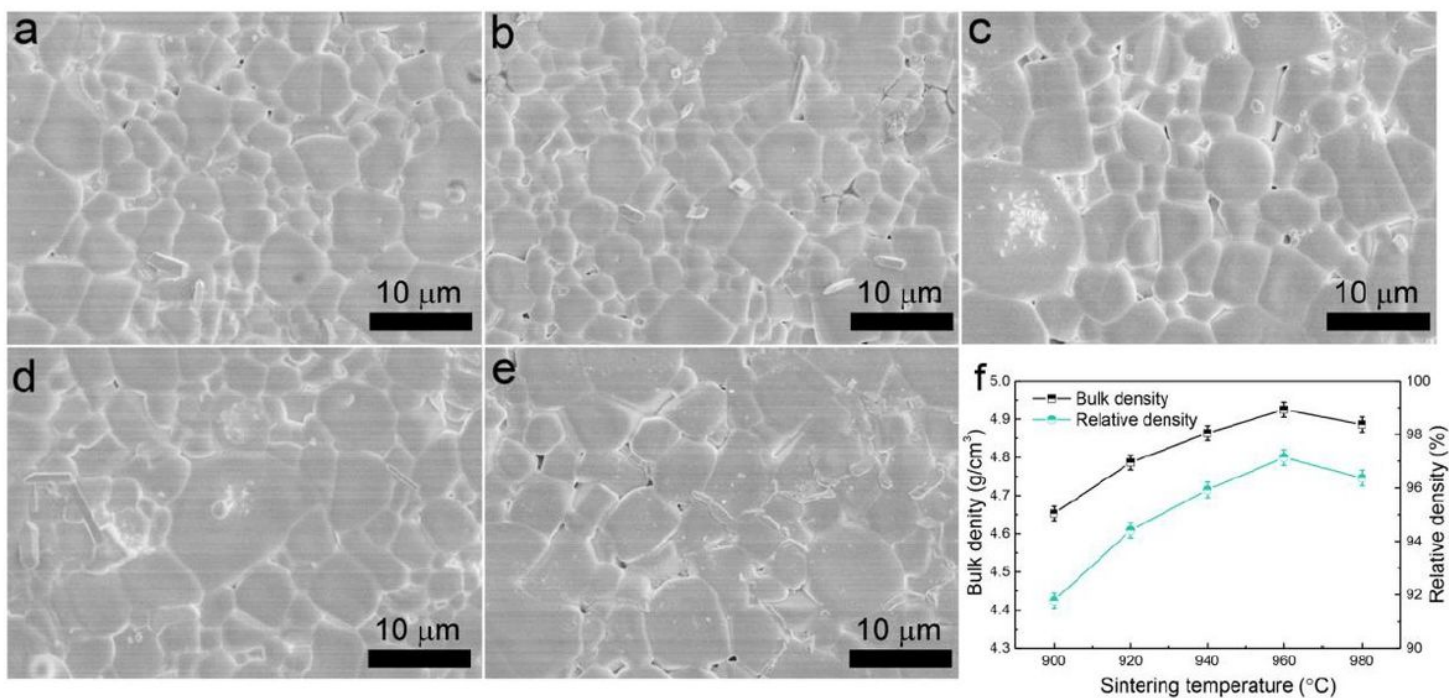


Figure 2

SEM micrographs of the polished and thermal etched surfaces of the Ba₂CuGe₂O₇ ceramics sintered at (a) 900 °C, (b) 920 °C, (c) 940 °C, (d) 960 °C, and (e) 980 °C; (f) the bulk density and relative density as a function of sintering temperature

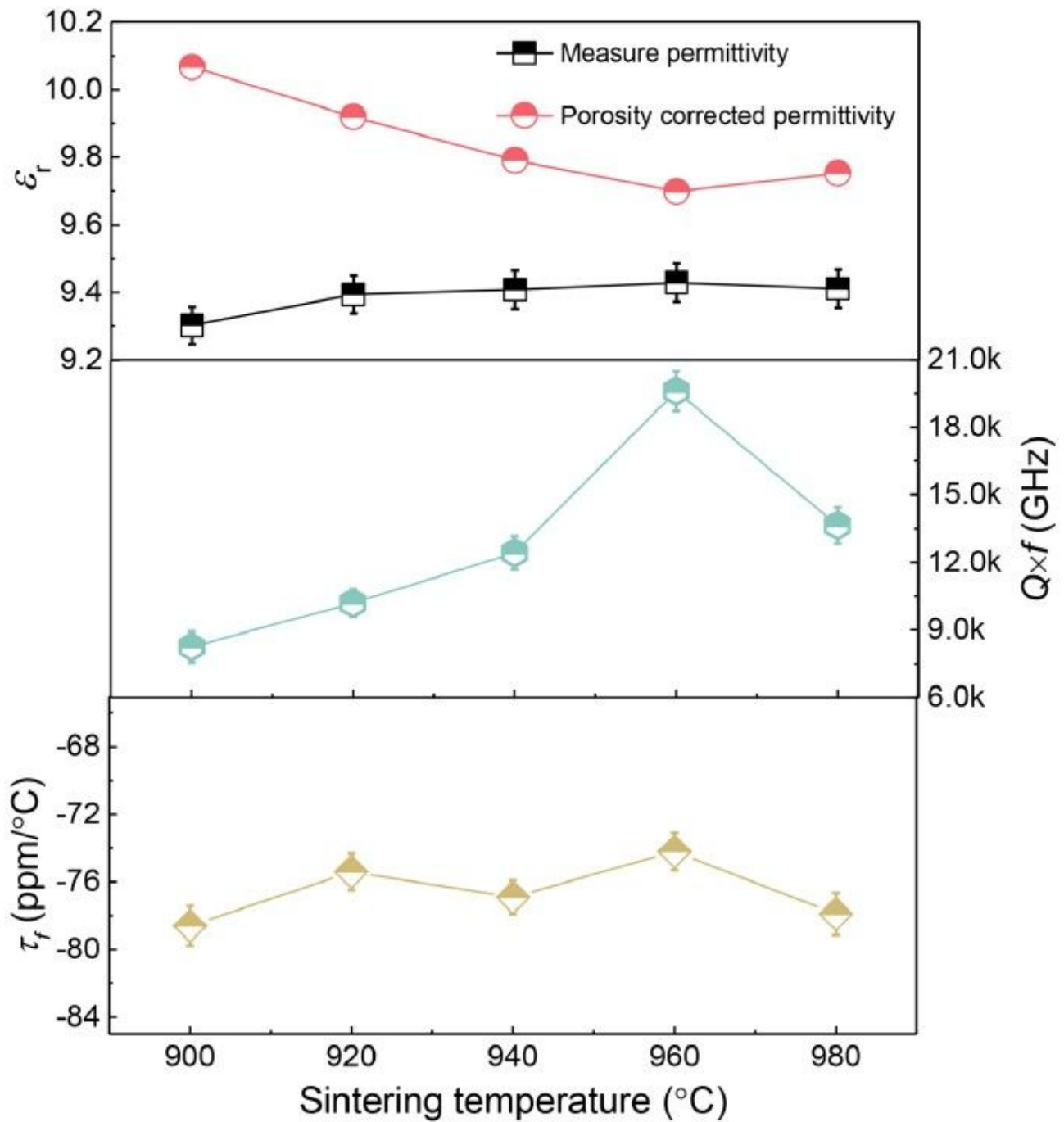


Figure 3

Microwave dielectric properties of Ba₂CuGe₂O₇ ceramics sintered at different temperatures (900- 980 oC)

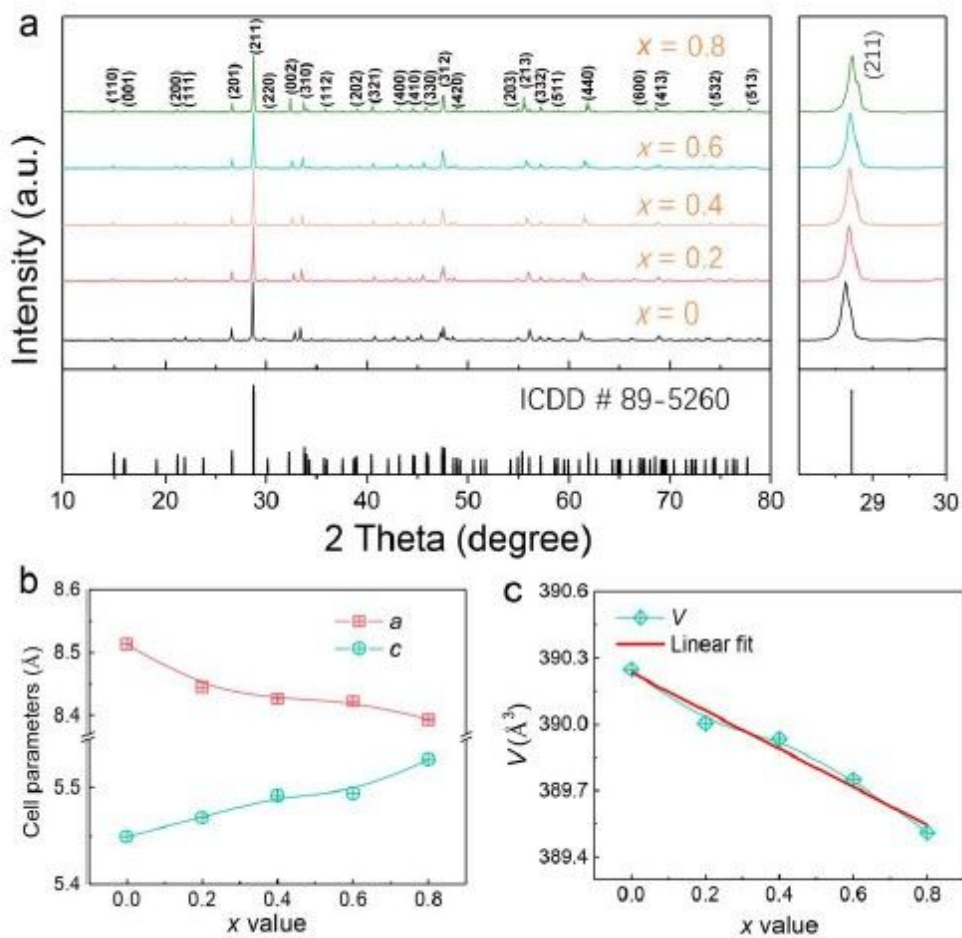


Figure 4

(a) Room-temperature XRD patterns for $\text{Ba}_2\text{Cu}_{1-x}\text{Mg}_x\text{Ge}_2\text{O}_7$ ($x = 0, 0.2, 0.4, 0.6, \text{ and } 0.8$) powders calcined at 900 °C; (b, c) variations in the lattice parameters as a function of composition x .

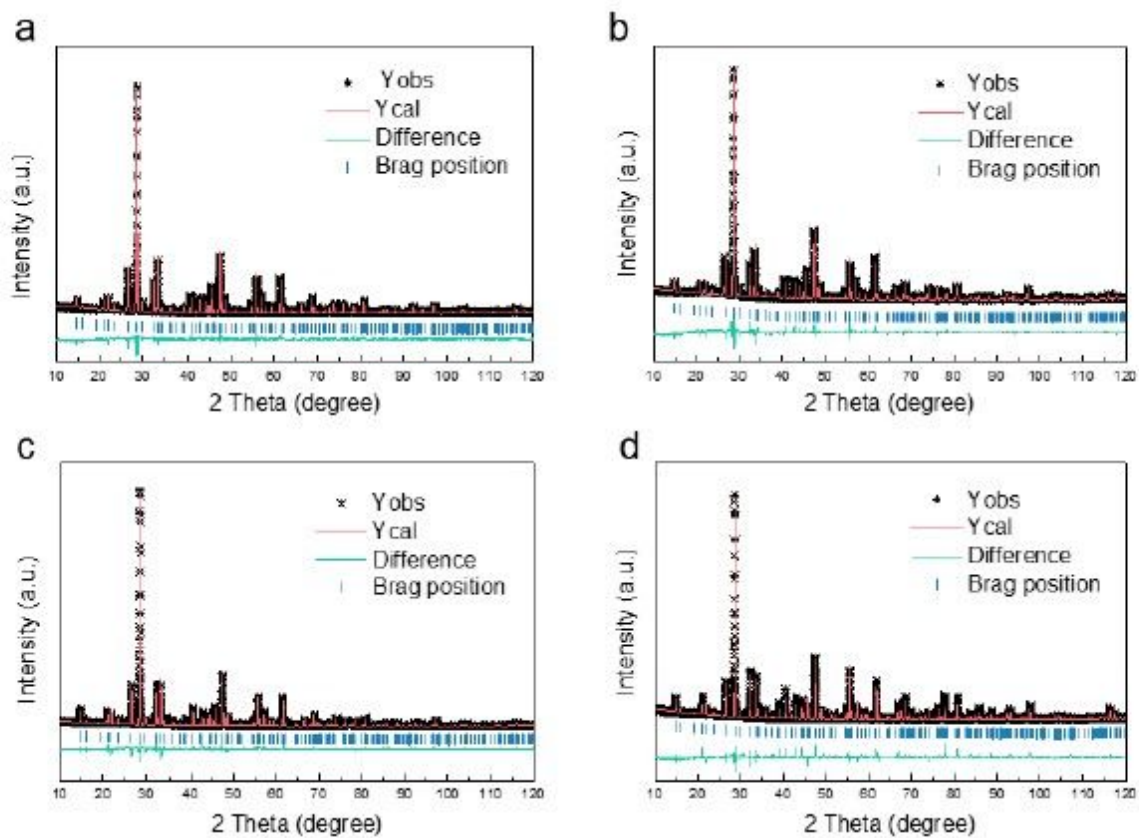


Figure 5

Rietveld refinement plots for $\text{Ba}_2\text{Cu}_{1-x}\text{Mg}_x\text{Ge}_2\text{O}_7$: (a) $x = 0.2$; (b) $x = 0.4$; (c) $x = 0.6$ and (d) $x = 0.8$.

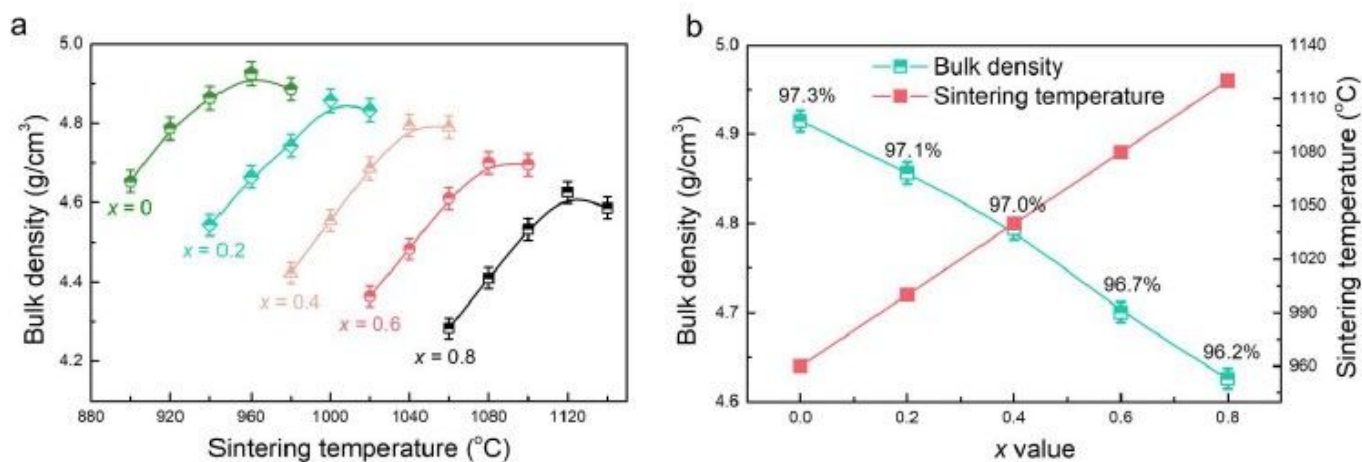


Figure 6

(a) Variations in bulk density as a function of sintering temperature for $\text{Ba}_2\text{Cu}_{1-x}\text{Mg}_x\text{Ge}_2\text{O}_7$; (b) the compositional dependence of bulk density and sintering temperature with the relative densities showing in the inset.

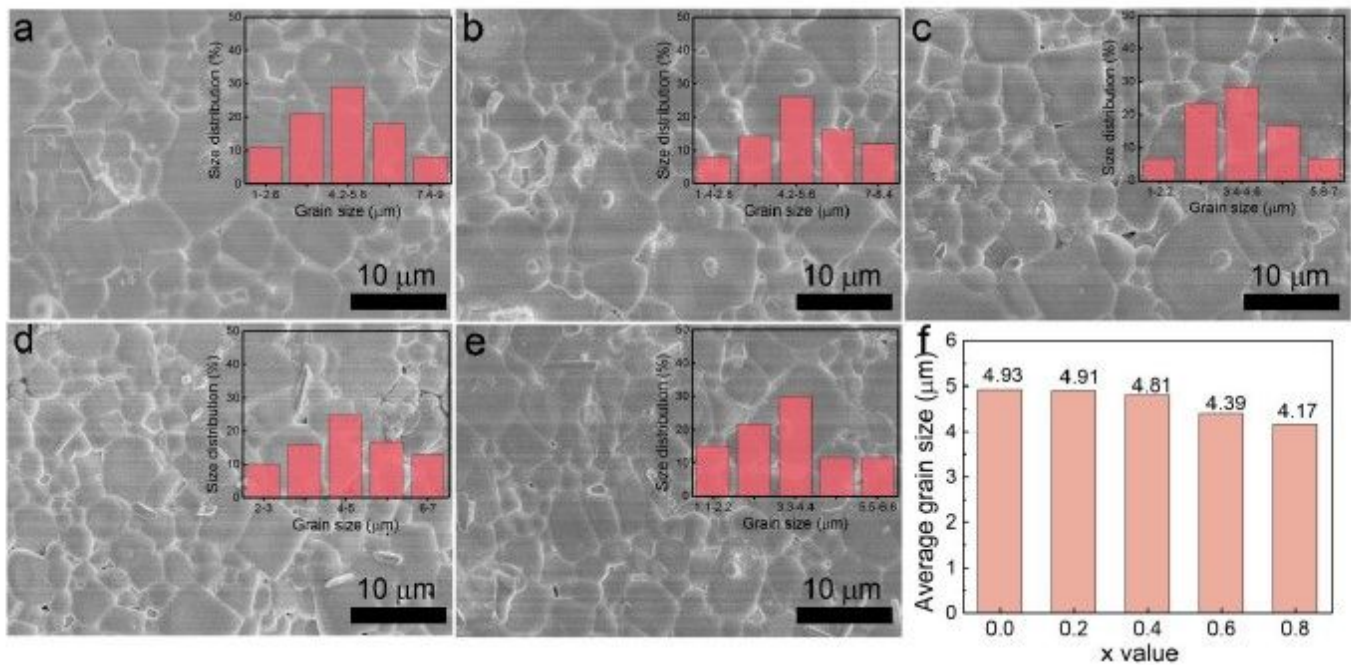


Figure 7

(a-e) SEM images and the grain size distributions for $\text{Ba}_2\text{Cu}_{1-x}\text{Mg}_x\text{Ge}_2\text{O}_7$ sintered at their optimum temperature; (f) the change of average grain size as a function of x value.

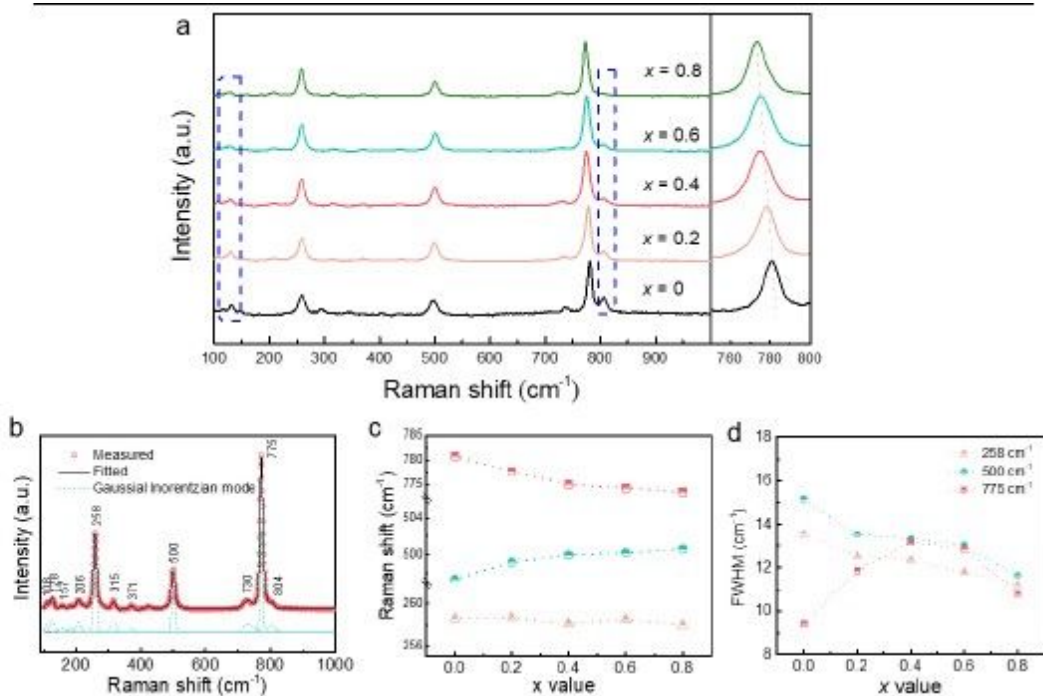


Figure 8

(a) Raman spectroscopies for $\text{Ba}_2\text{Cu}_{1-x}\text{Mg}_x\text{Ge}_2\text{O}_7$ along with an enlarged profile around $775\ \text{cm}^{-1}$; (b) a representative deconvolution fitting for the x = 0.8 composition; (c, d) variations in the Raman shift and FWHM for the three strongest Raman modes at $775\ \text{cm}^{-1}$, $500\ \text{cm}^{-1}$, and $258\ \text{cm}^{-1}$.

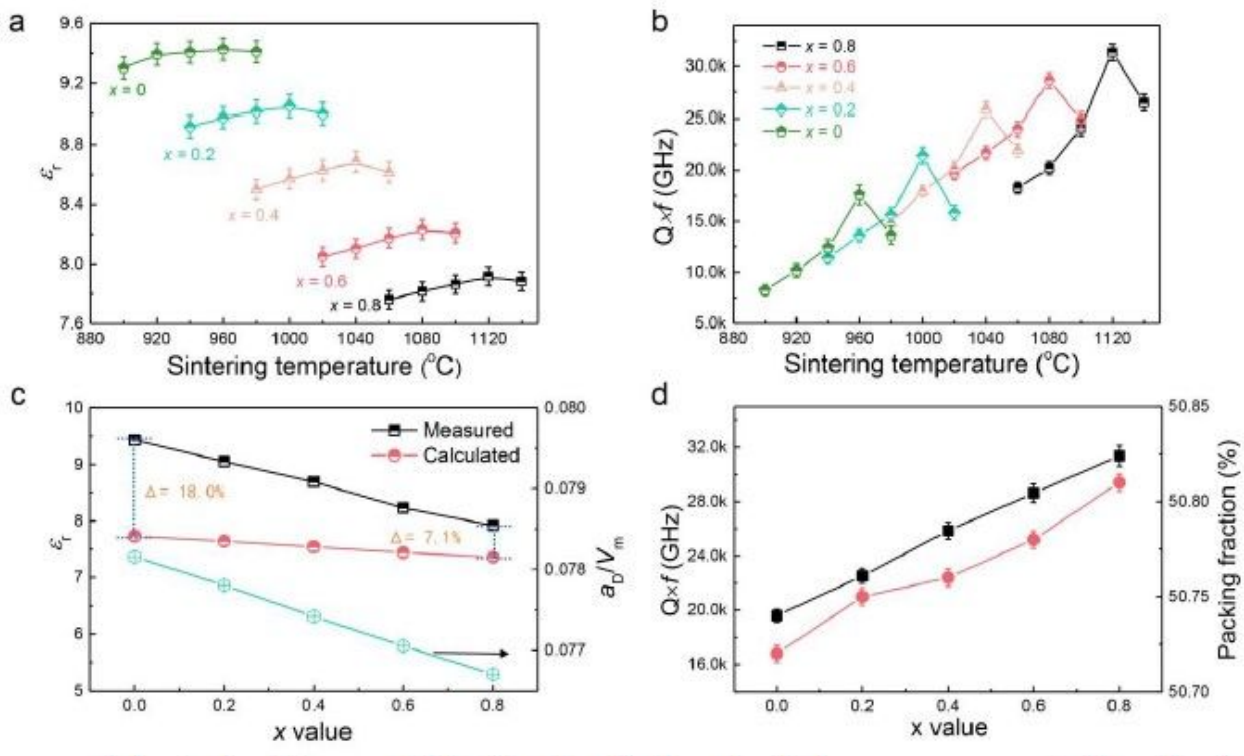


Figure 9

Variations in the relative permittivity (ϵ_r) and quality factor ($Q \times f$) of Ba₂Cu_{1-x}Mg_xGe₂O₇ (a, b) as a function of sintering temperature and (c, d) composition x value along with the change of the polarizability per unit volume ($a_D \cdot T / V_m$) and packing fraction.

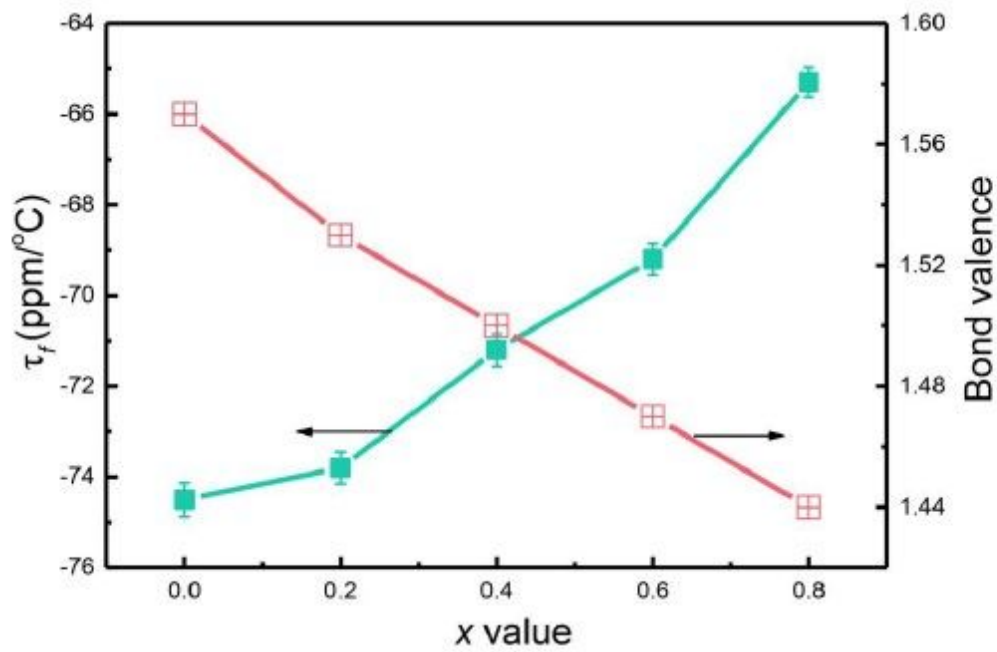


Figure 10

Variations in the temperature coefficient of resonance frequency (τ_f) and the bond valence of Mg/Cu-O.